View metadata, citation and similar papers at core.ac.uk

brought to you by CORE

provided by IntechOpen

We are IntechOpen, the world's leading publisher of Open Access books
Built by scientists, for scientists

4,800
Open access books available

122,000
International authors and editors

135M
Downloads

Our authors are among the

154
Countries delivered to

TOP 1%
most cited scientists

12.2%
Contributors from top 500 universities

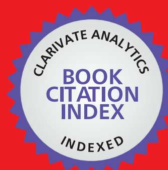

WEB OF SCIENCE™

Selection of our books indexed in the Book Citation Index
in Web of Science™ Core Collection (BKCI)

Interested in publishing with us?
Contact book.department@intechopen.com

Numbers displayed above are based on latest data collected.
For more information visit www.intechopen.com

Strain Effects in p-type Devices using Full-Band Monte Carlo Simulations

Valérie Aubry-Fortuna, Karim Huet*, T.T. Trang Nghiêm, Arnaud Bournel, Jérôme Saint-Martin and Philippe Dollfus
Institut d'Électronique Fondamentale, CNRS UMR 8622, Bât. 220, Univ. Paris-Sud, 91405 Orsay cedex,
**now at Excico France, 13-21 quai des Grésillons, Bât. B7, 92230 Gennevilliers, France*

1. Introduction

The particle-based Monte Carlo (MC) technique is acknowledged as a powerful method for accurately describing the carrier transport in semiconductor materials and devices within the semi-classical approximation, i.e. the Boltzmann transport equation (BTE) for the distribution function. It has been developed by many groups to study a wide variety of transport problems in many kinds of devices, to such a point that it is impossible to summarize here the most significant examples of its applications. The accuracy of the semiclassical transport description is then given by the models used for the band structure and the scattering mechanisms.

Hole transport properties in realistic Si devices are particularly affected by the strong anisotropy of the valence band (Thomson et al., 2006), which is further increased by the presence of strain. Analytic approximations fail to describe the valence band structure of Si, and an accurate or « full » description of the energy dispersion is then needed to describe hole transport correctly. In this work, the valence band structure is calculated thanks to a stress-dependent 30-band *k.p* model (Rideau et al., 2006). With this accurate valence band description, « Full-Band » Monte Carlo simulation becomes an appropriate tool to study various (unstrained or strained) p-type devices. Beyond the description of the model in Section 2, we show here two typical examples of application of the full-band Monte simulator to strain effects in p-type devices.

In Section 3, the influence of mechanical stress on Double Gate p-MOSFET performance is be investigated. Multiple gate structures are now recognized as promising architectures to overcome short channel effects in nanometer scaled MOSFET. Double Gate MOSFETs (DGMOS) are found to reach the best performance among SOI-based transistors (Saint Martin et al., 2006). In addition, mechanical stress is used as a technological performance booster for CMOS technology. The impact of stress on carrier transport is then of great importance and is both studied experimentally (Huet et al., 2008 ; Suthram et al., 2007) and theoretically (Huet et al., 2008a; Bufler et al., 2008; Pham et al., 2008). In this work, device performance of strained Si p-DGMOS is studied considering uniform biaxial and uniaxial stresses in the channel. The effect of strain is analyzed *via* some of the main usual figures of

merit for device comparison: on-state and off-state currents, subthreshold slope and intrinsic gate delay.
In Section 4, the giant piezoresistance effect is investigated in p-type silicon. The piezoresistance is defined as the change in electrical resistance under the effect of mechanical stress (Smith, 1954). Recently, an unexpected giant piezoresistance effect has been demonstrated experimentally in p-type Si nanowires (He & Yang, 2006). It could be used to achieve high performance MEMS sensors. High piezoelectric coefficients (up to about 3500×10^{-11} Pa^{-1}) were obtained for structures of high resistivity (i.e. lightly doped) and small diameter. It opens the way to the design and implementation of very small piezoresistive sensors, 5 to 10 times smaller than current MEMS components, with performance at least equal or even superior to those of the state of art. Some studies have attempted to explain the origin of this giant piezoresistance effect (Cao, 2008; Nakamura, 2009) which is not fully understood yet at the microscopic level. Hence, the theoretical understanding of this phenomenon by means of accurate simulation is of practical importance.

2. Monte Carlo and *k.p* models

2.1 Band structure calculations

Ab initio methods, such as the density functional theory, allow calculating the bandstructure from first principles (without any fitting parameters) to the price of large computational resources. More efficient semi empirical methods, involving fitting parameters, such as empirical pseudo-potentials (EPM), tight-binding (TB) or *k.p*, are more commonly used. The *k.p* method is based on the perturbation theory and some symmetry considerations (Rideau et al., 2006; Luttinger & Kohn, 1955, Cardona & Pollak, 1966; Richard et al., 2004). For a periodical lattice, the wave functions Φ_{nk} can be expressed in a periodical Bloch function basis (u_{nk}):

$$\Phi_{nk} = \exp(i\mathbf{k}.\mathbf{r})\, u_{nk}(\mathbf{r}) \tag{1}$$

where n is the band number, **k** the reciprocal lattice vector and **r** the real space position vector of the atoms.
Using Bloch theorem and assuming the eigenfunctions (wave functions) and eigenvalues (energies) at state $\mathbf{k} = 0$ are known, the Schrödinger equation writes:

$$H_k u_{nk} = \left(H_0 + \frac{\hbar}{m_0}\mathbf{k}.\mathbf{p} + \frac{\hbar^2 |\mathbf{k}|^2}{2m_0} \right) u_{nk} = E_{nk} u_{nk} \tag{2}$$

where H_0 is the Hamiltonian at $\mathbf{k} = 0$, m_0 the free carrier mass, **p** the carrier momentum and E_{nk} the energy associated with carrier wave vector **k** and band n.
The Hamiltonian H is projected on a truncated basis, here a given number N of the Zinc-Blende Γ-centered Bloch functions, and the resulting matrix is diagonalized to obtain the eigenenergies and wave functions at **k** for the N bands. Adding spin-orbit interaction gives a better description of the bandstructure but doubles the size of H. The matrix elements of H depend on interband coupling parameters and eigenenergies at $\mathbf{k} = 0$. The empirical parameters used are the band gap and known effective masses around specific **k**-points. The accuracy and the **k**-space range of validity of the resulting bandstructure depend on the

number of bands taken into account (i.e. the number of Bloch functions of the truncated basis). When "full-zone" *k.p* methods are considered, including up to 30 bands or more with spin-orbit coupling as done in this work, a great number of interband coupling parameters is needed. Due to the lack of experimental data, they are determined by comparison to ab initio calculations. To include mechanical stress in the calculation, the other band methods (EPM, TB) treat the strained crystal as a new system. However, taking strain into account in the *k.p* formalism, as first introduced by Bir and Pikus (Bir & Pikus, 1974), is straightforward using correctly adjusted deformation potentials (Rideau at al., 2006).

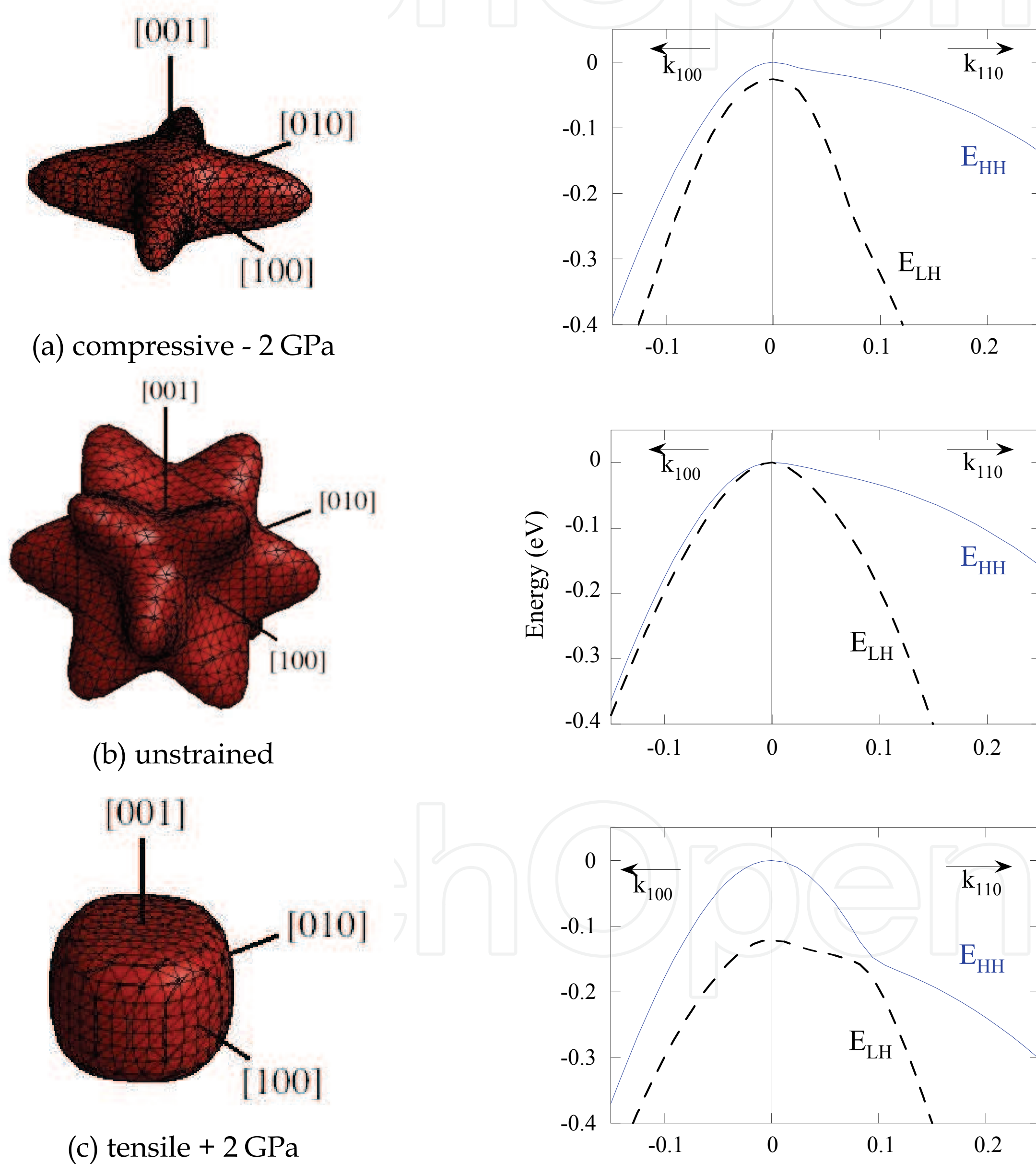

Fig. 1. Si bandstructures obtained using 30 band *k.p* method with and without strain. On the left: constant energy surface at 40 meV from band edge for the 1st hole band (heavy holes). On the right: corresponding E(k) (eV) in [100] and [110] directions for the 1st (HH) and 2nd (LH) bands. (a) Compressive strain - 2 GPa, (b) unstrained, (c) tensile strain + 2 GPa.

The influence of biaxial strain can be seen on Fig. 1. For unstrained Si, the "heavy hole" (HH) band (hereafter called the 1st band) shape is very anisotropic and the "light hole" (LH) band (hereafter called the 2nd band) shape is more isotropic. Under strain, the degeneracy at the Γ point is lifted. For compressive strain, the nature of the bands is similar to the unstrained case. For tensile strain, the nature of the bands is inverted at low energy and returns to the unstrained case shape at higher energies. For the 2nd band, the effective mass in the [100] direction does not vary significantly with strain. For the 1st band, it shows a 20% decrease under compressive strain and a 3% decrease under tensile strain.

2.2 Monte Carlo code

MONACO is a self consistent particle MC device simulator (Aubry-Fortuna et al., 2006) coupled with a 2D Poisson equation solver. We consider scattering mechanisms related to elastic acoustic phonons, inelastic optical phonons, ionized impurities and SiO_2/Si surface roughness. The latter is accounted for via an empirical combination of diffusive and specular reflections (50% of diffusive reflections for holes). The Newton propagation equations during free flights are solved numerically with a first order Runge Kutta scheme (Laux & Fischetti, 1991). The anisotropy of the bandstructure is taken into account in the choice of the state after scattering by considering the "local" density of states in reciprocal space as done in (Jungemann et al., 1999).

The phonon scattering rates are energy-dependent and proportional to the density of states calculated from the full bandstructure. The optical phonon energy is 63 meV. The acoustic ($D_{AC}/c_s = 7.72\ 10^{-4}$ eV.m^{-1}.s, c_s being the average sound velocity in bulk Si) and optical ($D_{OP} = 7.1\ 10^8$ eV.cm^{-1}) phonon deformation potentials have been slightly adjusted to reproduce the experimental velocity as a function of applied field characteristics of bulk unstrained Si (Ottaviani et al., 1975; Huet et al., 2008b). The impurity scattering rate is calculated using an analytical approximation as in (Aubry-Fortuna et al., 2006).

3. p-DGMOS performance

The typical simulated device characteristics are the following: gate length L_G = 21 nm, channel length L_{ch} = 19 nm, physical gate oxide thickness T_{ox} = 1 nm, Si body thickness T_{Si} = 8 nm, metallic midgap gate material with a workfunction Φ_m = 4.56 eV, supply voltage V_{DD} = 0.9 V. The undoped channel is <100> or <110>-oriented on a (001) wafer. The N+ doping level in the source and drain extensions is 10^{20} cm^{-3} and abrupt doping profiles at source-channel and channel-drain junctions are considered. The source (or drain) access length L_{spac} is 80 nm, which corresponds to a total access resistance of about 230 Ω.cm. The simulations of the devices have been performed considering a uniform biaxial strain in the (100) plane or a uniaxial strain along <110> or <-110>, with stress values ranging from -0.5 GPa (compressive) to +1 GPa (tensile).

3.1 Current-voltage characteristics

Drain current I_D as a function of gate voltage $-V_{GS}$ characteristics at low drain voltage V_{DS} (= -0.05 V) and high V_{DS} (= $-V_{DD}$ = -0.9 V) have been simulated for all devices. The threshold voltage V_T is determined from the $I_D(-V_{GS})$ curves, using the constant current method with I_D = 10 μA/μm as the reference current obtained at low V_{DS} (-0.05 V) and not in saturation (-0.9 V). To clearly evidence the impact of strain, values of the on-state current I_{on} are compared at the same gate overdrive (V_T - V_{GS}), which corresponds exactly to V_{GS} = -0.9 V in

the case of unstrained device. Some of the typical $I_D(V_T - V_{GS})$ characteristics at V_{DS} = 0.9V are reported in Fig. 2.

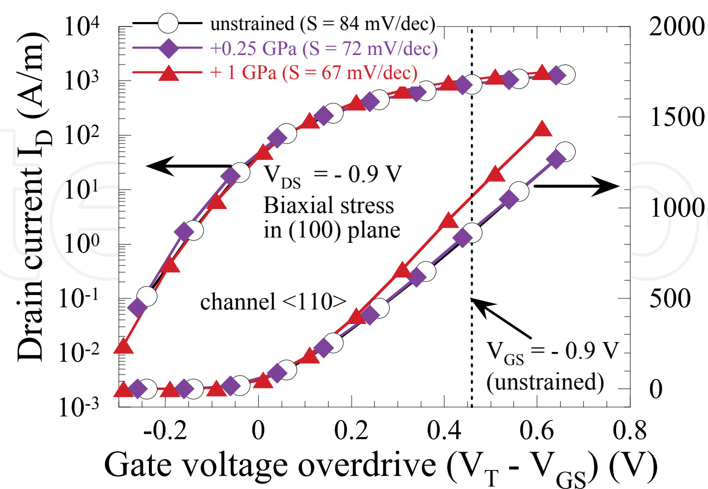

(a)

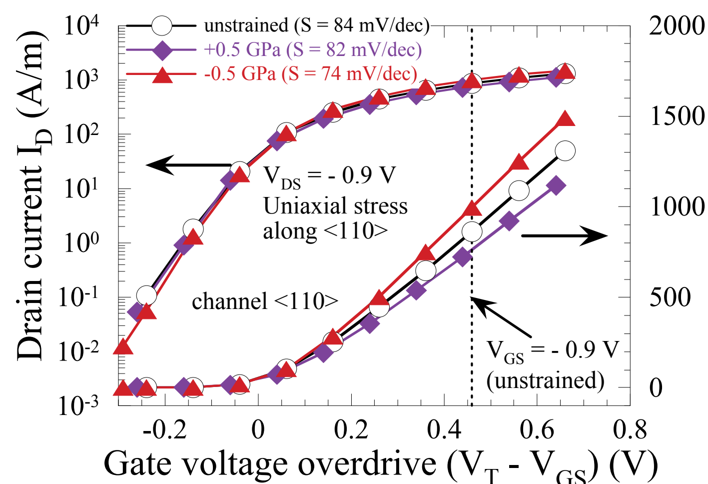

(b)

Fig. 2. $I_D(V_T - V_{GS})$ characteristics at high V_{DS} for: (a) a biaxial stress in the plane (100) and (b) a uniaxial stress along <110>. The channel is oriented along the <110> direction. Values of subthreshold slopes are indicated in the legends.

According to these results and to the other characteristics not shown here, the strain - biaxial or uniaxial, tensile or compressive - is systematically beneficial to the subthreshold slope S, certainly due to strained-induced splitting of valence bands. The lowest improvement of S is obtained for a uniaxial stress along <110> with a <110>-oriented channel: S varies from 84 mV/dec for unstrained to 82 mV/dec for +0.5 GPa (as indicated in Fig. 2b). However, in the case of a biaxial stress with the same channel orientation, S is strongly improved and decreases down to 67 mV/ dec for +1 GPa (see Fig. 2a). In Fig. 3, on-state currents (at the same gate overdrive) are reported as a function of stress for all studied devices. Under a tensile biaxial strain (Fig. 3a), the current I_{on} always increases and the highest values are obtained for a <100>-oriented channel. Indeed, in the unstrained case, due to the anisotropy

of the valence band stucture, the heavy hole mass is lower in the <100> direction than in the <110> one, which is advantageous for transport and yields a higher on-state current (see the symbols at 0 GPa in Fig. 3a). Applying a biaxial stress in the plane (001) induces an important degeneracy lift between heavy hole (HH) and light hole (LH) bands (30 meV for +0.5 GPa and ≈ 55 meV for +1 GPa (Huet, 2008)). It also makes the HH band more isotropic with lower HH masses than in the unstrained case, leading to a systematic improvement in current (as it can be seen in Fig. 3a). In addition, quasi-ballistic transport has been previously studied in such devices (Huet et al., 2008b). The hole transport is obviously non-stationary. The fraction of ballistic holes (non-scattered holes when crossing the channel), also called intrinsic ballisticity, is quite low in these devices (about 10%) and remains nearly strain independent (maximum of 12%). The average number of scatterings N without strain is also low (N ≈ 4) and variations with strain is less than 10% (for more details, see (Huet, 2008)). Hence, in the case of a tensile biaxial stress, the drive current variation is mostly due to band curvature improvement.

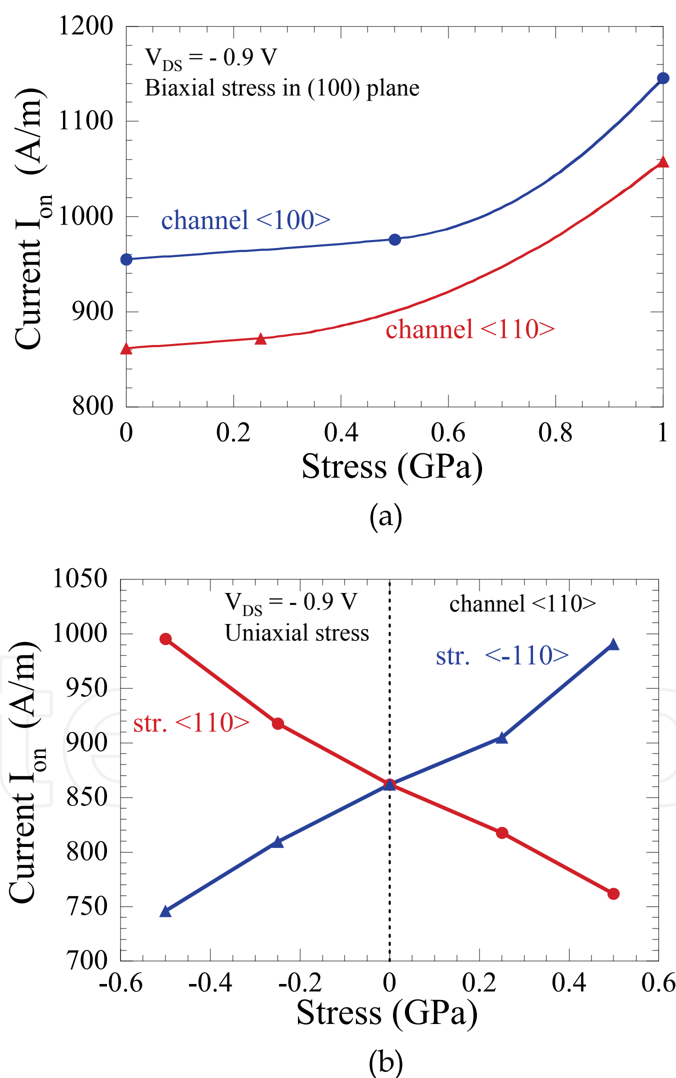

Fig. 3. Variation of the on-state current I_{on} at the same gate overdrive as a function of: (a) biaxial stress in the (100) plane (the two channel directions are represented), and (b) uniaxial stress along <110> and <-110> (the channel direction is <110>).

Under uniaxial stress (Fig. 3b), both compressive stress along <110> (channel direction) and tensile stress along <-110> improve the on-state current. The opposite behaviour is observed under tensile and compressive stress, respectively. The behaviour of the on-state current as a function of stress is also related to hole mass variations. For example, for a uniaxial stress along <110>, the valence band structure remains anisotropic and the compressive stress is the most advantageous case, while it greatly decreases the heavy hole mass in the <110> direction (compared to the tensile one). Concurrently, the compressive stress increases the LH mass, but due to the degeneracy lift (≈ 25 meV for -0.5 GPa), it remains beneficial for hole transport and is then responsible for the I_{on} improvement shown in Fig. 3b. In addition, the number of scattering events has been analyzed. For the same example as previously (uniaxial stress along <110>) and contrary to the biaxial stress case, the intrinsic ballisticity decreases progressively when tuning the stress from -0.5 GPa to +0.5 GPa. As a consequence, the average number of scatterings N varies from ≈ 3.5 to ≈ 6 in the same stress range. The average mean free path of holes, defined as L_{ch}/N, decreases and is then perfectly correlated to the on-state current (Huet, 2008). Unlike the biaxial stress case, the variation of interband phonon scattering with strain (correlated to band splitting) plays a role as important as the band curvatures on the enhancement or degradation of on-state current.

3.2 Comparison with experimental mobilities and currents

On-state current variations have been compared to experimental data (Huet et al., 2008a; Rim et al., 2003) and the results are reported in Fig. 4. For uniaxial stress, variations of mobility and of on-state current are similar though quantitatively different. In addition, for stress along <110>, the calculated I_{on} variations are in fairly good agreement with experimental currents obtained for long channel transistors under bending (Fig. 4b, red diamonds) (Huet et al., 2008a). For biaxial stress, variations of mobility and I_{on} are quite different.

First, as observed in ultra-short devices, on-state current variations are often lower than the long-channel mobility ones (see e.g. (Aubry-Fortuna et al., 2006) for the impact of biaxial strain in bulk n-MOS). Second, using the Kubo-Greenwood formalism (KG), mobilities in inversion layers have been previously calculated and compared to results from wafer bending experiments (Huet et al., 2008a). The experimental trends are correctly reproduced using a 3D hole gas description (KG 3Dk) for uniaxial stresses along <110> and <-110> in <110>-oriented channels, but it was shown that quantum confinement (KG 2Dk) has to be taken into account in the calculation to fit with long-channel mobility variations in the biaxial case. Using full-band simulation including quantization, I-V characteristics have been very recently reported for uniaxially-strained short-channel p-DGMOS but for a high stress value (-2 GPa), which makes the comparison with our results difficult (Pham et al., 2008). The problem of the actual influence of quantization effects in strained transistors is thus still open. Nevertheless, it was shown that, in ultra-short devices with highly non-stationary transport quantum, confinement effects are small except in the case of biaxial tensile strain (Wang et al., 2006) for which bulk band results may overestimate the strain influence. Therefore, the results for biaxial strain should be considered cautiously. It is shown at least that, though it remains a modelling issue, in the early phase of technology development of aggressively scaled DGMOS including strain-engineering, the key figures can be given by standard full-band Monte Carlo simulation.

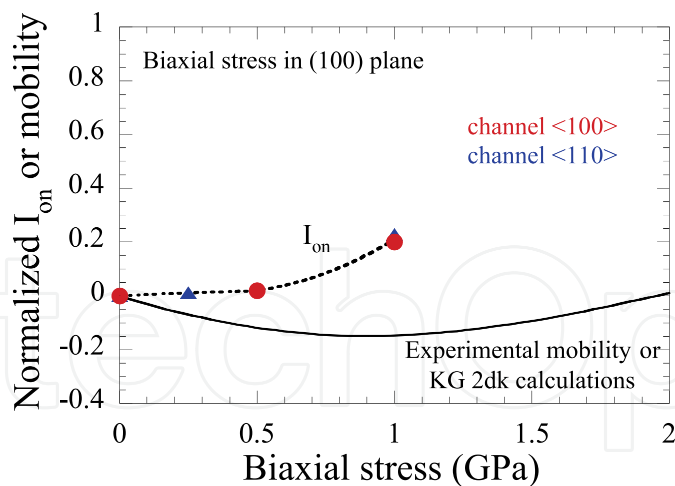

(a)

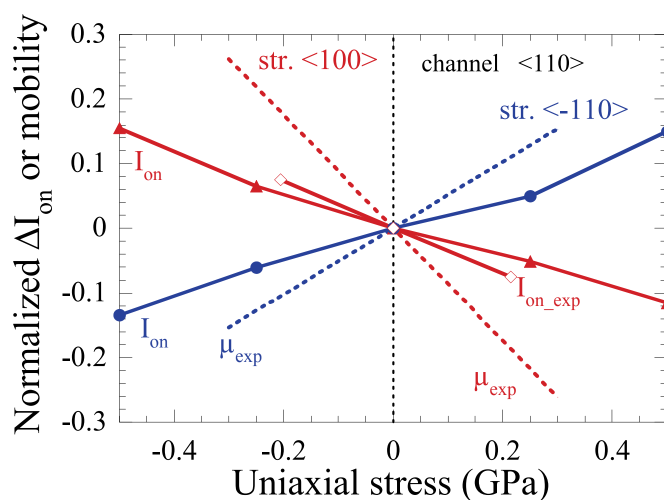

(b)

Fig. 4. Normalized I_{on} (relative to unstrained device) as a function of: (a) biaxial strain with experimental mobility from (Rim et al.,2003) and Kubo-Greenwood 2dk calculations (Huet et al.,2008); and (b) uniaxial strain with experimental mobility and current from (Huet et al., 2008).

3.3 Figures of merit

Intrinsic gate delay $C_G V_{DD}/I_{on}$ and off-state current I_{off} are considered as important figures of merit for CMOS applications. The intrinsic gate capacitance C_G is extracted from the Monte Carlo simulation results, as the derivative of the total charge in the device with respect to V_{GS} at low V_{DS}. The off-state current is determined at the same gate overdrive (V_T - V_{GS}), which corresponds to V_{GS} = 0 V in the case of unstrained device and is then equal to -0.44 V. Intrinsic gate delays and off-currents are often compared to ITRS specifications (ITRS, 2008) which fix the device performance objectives (Fig. 5). Nevertheless, it is to be noted that ITRS delay values are for n-MOSFET and the ones for p-MOSFET should be probably higher.

All off-state currents are lower than the maxima defined by the ITRS specifications. Most of the devices exhibit delay values lower than the LSTP40 specifications, except the two ones

that have the lowest on-state currents as shown in Fig. 3b (tensile stress along <110> and compressive stress along <-110>). Performance of the unstrained and strained devices studied here is quite satisfactory according to the 2008 ITRS recommendations. Let's remark that the ITRS access resistance for source and drain access is estimated to be around 180-190 Ω.µm. The total access resistance in our simulations is higher (230 Ω.µm), which leads to under-estimated on-state currents, and then to overestimated delay values.

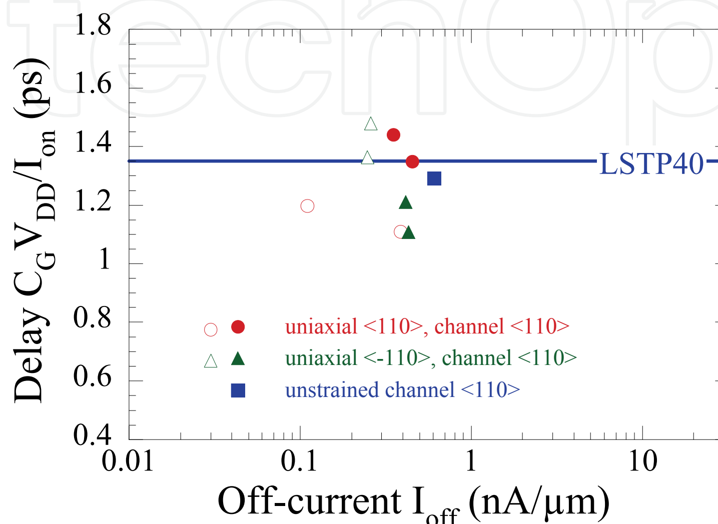

Fig. 5. $C_G V_{DD}/I_{on}$ variations for all uniaxially stressed p-DGMOS. Specifications of ITRS'2008 are also reported. Open symbols are for various compressive stresses and solid ones for various tensile stresses.

4. Giant piezoresistance effect in p-Si nanowires

A nanowire is essentially a three-dimensional object. However, in a first approach to the problem of giant piezoresistance and to reduce the computation time, we restricted ourselves to the consideration of silicon nano-layers of infinite width described in 2D real space. The effect of stress on the surface potential is applied on both sides of the nano-layer. In nanostructures, the size quantization effects may be very important. Several works on silicon nanowires have shown that these effects may influence substantially their electrical and mechanical properties. In particular, for diameter smaller than 20 nm, many physical quantities such as the Young's modulus, the Poisson ratio, the electron and hole effective mass, the band gap and the mobility are strongly affected with respect to bulk data (Leu et al., 2006; Leu et al., 2008; Ghetti et al., 2007). However, in this study, to compare with available experimental data, we simulated structures with minimum thicknesses of 80 nm which is much larger than the critical size mentioned above. Quantization effects are thus safely neglected here.

4.1 Simulated structures

All simulated structures have an effective length of 500 nm. The thickness d is 80 nm, 100 nm or 150 nm. The p-type Si layer is doped to 10^{18} cm^{-3}, 2.7×10^{17} cm^{-3} or 1.49×10^{16} cm^{-3}, which corresponds to a bulk resistivity of 0.044 Ω.cm, 0.1 Ω.cm and 1 Ω.cm, respectively. At

both ends, the Si layer is overdoped to 10^{19} cm^{-3} and contacted by an Ohmic contact which injects/ detects the flux of particles flowing through the structure. The uniaxial stress is uniformly applied along the [110] transport direction. The surface potential φ is defined as the difference in the top of valence band between the surface and the volume of the material where neutrality is assumed to be recovered. The effect of stress is modeled along the line proposed by Rowe who investigated the giant piezoresistance effect in Si nanowires using a very simple approach of transport (Rowe, 2008). For a uniaxial stress X, the surface potential φ varies according to the law

$$\frac{d\varphi}{dX} = 0.5 \ \text{meV/MPa} \tag{3}$$

considering that for unstrained Si, φ_0 = 0.54 eV. The nano-layers are simulated under a bias voltage of 0.5 V for stresses ranging from 0 to ± 100 MPa applied along the <110> crystallographic direction.

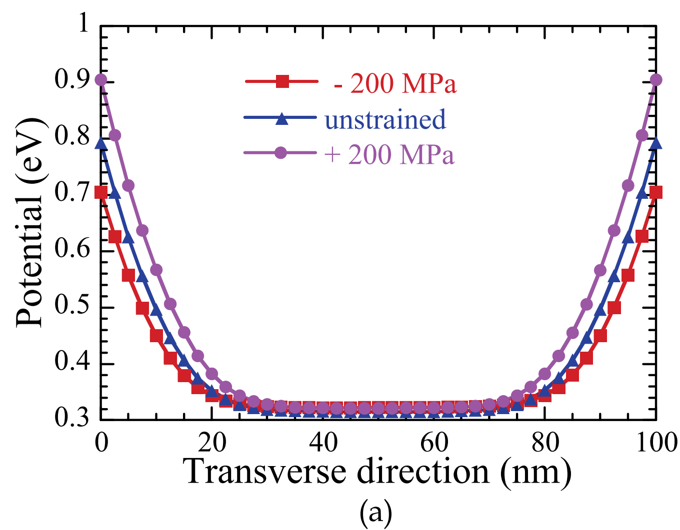

(a)

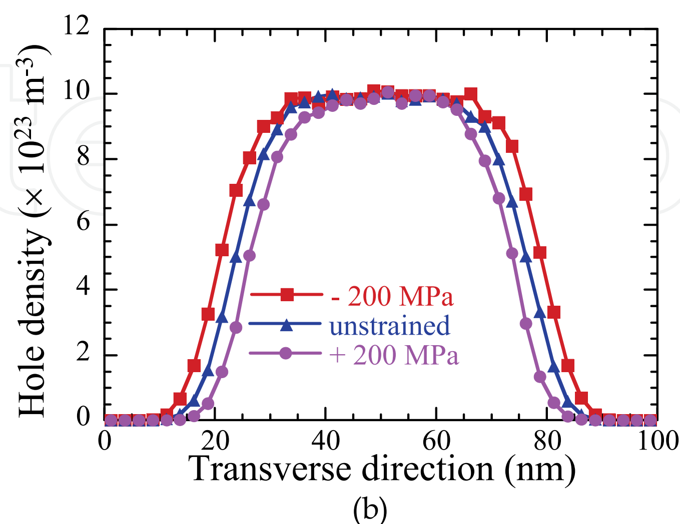

(b)

Fig. 6. (a) Potential and (b) hole density profiles in a 100 nm-thick Si layer of resistivity 0.044 Ω.cm for three stress conditions.

4.2 Potential and hole density profiles

According to Eq.(3), the surface potential is reduced under tensile strain while it is enhanced under compressive strain. Fig. 6a shows the typical potential profile in the middle of the device along the transverse direction for three values of stress and a small resistivity ρ = 0.044 Ω.cm. The stress essentially modulates the depth of the surface depleted region, while the potential in the center of the structure remains unchanged and equal to its equilibrium position. Accordingly, the maximum hole density remains equal to the impurity concentration in the central region. The stress controls only the width of this neutral region, i.e. the conductive area, as shown in Fig. 6b. The situation is different for a higher resistivity ρ = 0.1 Ω.cm, as shown in Fig. 7. Due to lower doping concentration, the depleted region extends more deeply in the structure and the potential does not fully recover its equilibrium position (Fig. 7a). Accordingly, there is no longer any neutral region in the device and the stress not only controls the width of the conductive area but also the height of the potential barrier for holes and the maximum hole density (Fig. 7b). These results are in qualitative agreement with experimental C-V measurements on nanowires (Garnett et al., 2009).

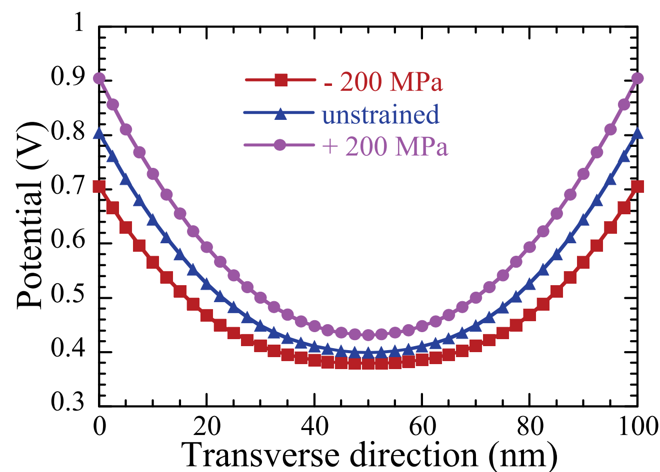

(a)

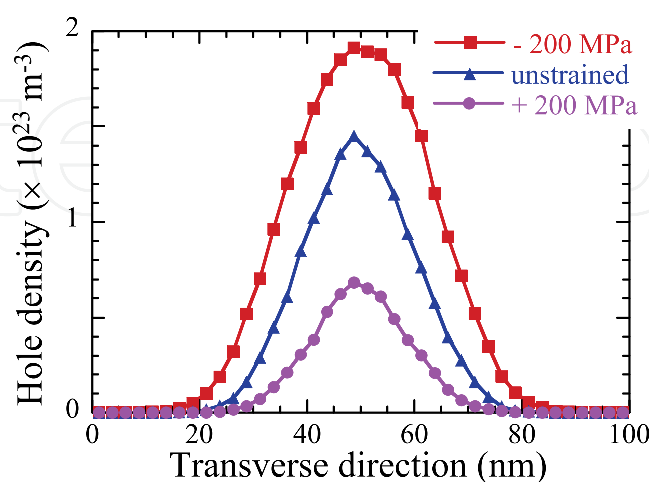

(b)

Fig. 7. (a) Potential and (b) hole density profiles in a 100 nm-thick Si layer of resistivity 0.1 Ω.cm for three stress conditions.

4.3 Current and piezoresistive coefficients

Fig. 8 shows the current in the nano-layers as a function of stress for a thickness of 100 nm and various resistivity values. In the low-resistivity structure (ρ = 0.044 Ω.cm), the current is controlled by the width of the conductive area and is linearly dependent on stress. For higher resistivities (ρ = 0.1 Ω.cm and 1 Ω.cm), the current is much smaller and controlled by the height of the potential barrier in the centre of the structure, which leads to a quasi-exponential dependence of the current as a function of stress.

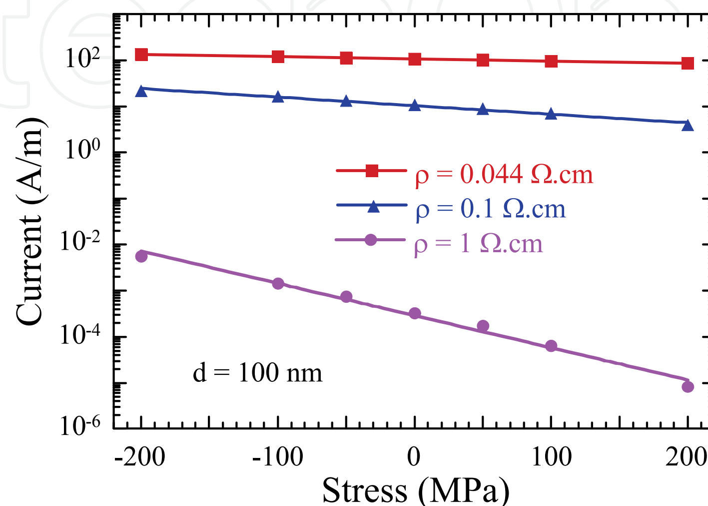

Fig. 8. Current versus stress in nano-layers of 100 nm-thickness for different resistivities. For the two highest resistivities, the solid lines are exponential fitting curves.

To quantify the piezoresistive phenomenon, the most relevant factors of merit are the relative variation of conductivity $\Delta\sigma/\sigma_0$ and the longitudinal piezoresistive coefficient π_1^{σ}. The relative change in conductivity $\Delta\sigma/\sigma_0$ for <110> nanowires is directly deduced from the relative change in conductance $\Delta G/G_0$ using the following equation (see Supplementary Information of (He & Yang, 2006)):

$$\frac{\Delta\sigma}{\sigma_0} = \frac{\Delta G}{G_0} + (0.84 \times 10^{-11}\,\mathrm{Pa}^{-1})X \tag{4}$$

Some results of relative change in conductivity $\Delta\sigma/\sigma_0$ as a function of stress are shown in Fig. 9 for three thicknesses of 80, 100 and 150 nm and three resistivities of 0.044, 0.1 and 1 Ω.cm.

To separate the contributions of stress-induced changes in the valence band structure and in the surface potential, we first considered the only effect of surface potential modulation while keeping the band structure of unstrained Si. The effect of stress on the band structure was considered in a second stage. The comparison of the solid and dashed lines in Fig. 9a shows that both contributions of the potential surface variation and of the change in bands must be taken into account, though the latter smaller, especially in the case of thin layers. The change in conductivity is not always linear and depends strongly on both the doping level and the thickness (that is to say, the diameter in the case of a nanowire). At a given resistivity, the variation $\Delta\sigma/\sigma_0$ as a function of stress is higher and more nonlinear when reducing the layer thickness. The amplitude of variation of conductivity obviously increases when increasing the resistivity (see Fig. 9b).

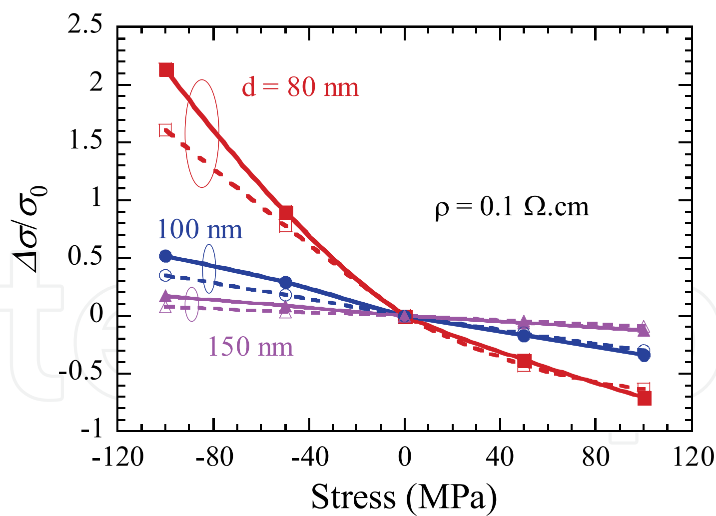

(a)

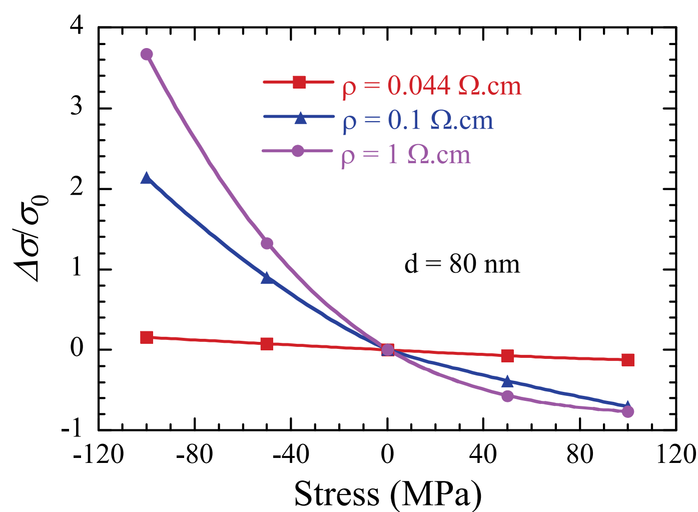

(b)

Fig. 9. Relative variation of conductivity $\Delta\sigma/\sigma_0$ as a function of stress for different thicknesses and resistivities, and with (solid lines) or without (dashed lines) change in band-structure. (a) ρ = 0.1 Ω.cm and (b) d = 80 nm.

For a high resistivity of 1 Ω.cm, the relative change of conductivity as a function of stress seems to be nearly independent of the layer thickness, as shown in Fig. 10. This is probably associated with the fact that the current in a quasi-fully-depleted region is exponentially controlled by the potential barrier whatever the thickness, which makes the stress-dependent change of relative conductivity weakly dependent of thickness. Overall, these results are in agreement with trends observed experimentally by He and Yang for nanowires (He & Yang, 2006).

The corresponding piezoresistive coefficients were calculated around X = 0 using the following expression

$$\pi_1^{\sigma} = \frac{1}{\sigma_0}\frac{d\sigma}{dX} \tag{5}$$

where σ_0 is the conductivity under zero stress.
The resulting piezoresistive coefficients are summarized in Table 1. As expected, they are strongly dependent on the nano-layer thickness and resistivity. A large piezoresistive coefficient of 1750×10^{-11} Pa^{-1} is obtained for a 80 nm thick layer with resistivity of 1 Ω.cm. The results obtained are quite consistent with experimental results of He and Yang (He & Yang, 2006). For instance, they obtained a first order piezoresistive coefficient of 660×10^{-11} Pa^{-1} for a 75 nm thick <110> oriented nanowire with resistivity of 0.3 Ω.cm. The highest piezoresistive coefficient measured was 3100×10^{-11} Pa^{-1} for a nanowire with resistivity of 102 Ω.cm. Accurate MC calculation in such a high resistivity layer is very difficult because of very small current level.

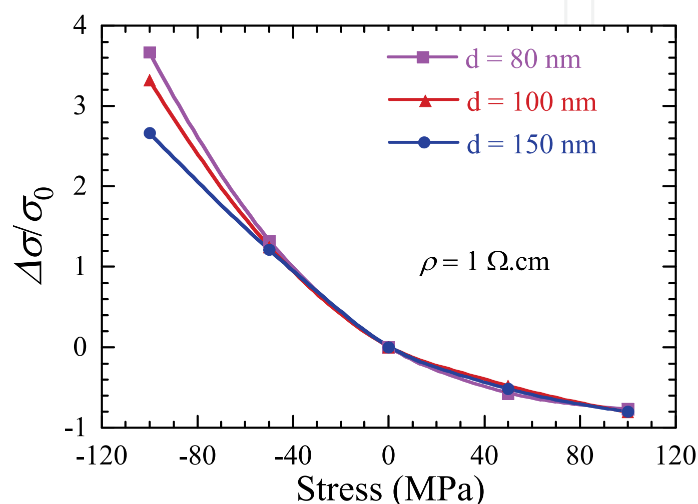

Fig. 10. $\Delta\sigma/\sigma_0$ as a function of stress for the resistivity of 1 Ω.cm and for different thicknesses.

Thickness d (nm)	Piezoresistive ρ = 0.044 Ω.cm	coefficients ρ = 0.1 Ω.cm	($\times 10^{-11}$ Pa^{-1}) ρ = 1 Ω.cm
80	141	842	1750
100	111	420	1589
150	80	149	1564
200	60	105	1505

Table 1. Piezoresistive coefficients in p-type <110>-oriented Si nano-layers for different thicknesses and resistivities.

5. Conclusion

We have presented a full-band particle Monte Carlo simulator based a 30 band *k.p* bandstructure calculation, and two typical applications to p-type silicon nanodevices. First, the advantage of introducing compressive and tensile stresses in ultra-thin p-type Si DGMOS has been discussed in the case of biaxially and uniaxially strained <100> and <110>-oriented channels. The strain-induced improvement of device performance has been highlighted when devices are compared at the same gate overdrive. The performance indicators agree quite well with specifications of the updated 2008 ITRS defined for LSTP40

technology node. Second, we have investigated the giant piezoresistance effect in p-type Si nanolayers of 80 – 150 nm thickness which are assumed to behave as nanowires. This effect is mainly due to the strain-induced modulation of the surface potential. The effective conduction area, wide in the case of compression, becomes much narrower in the case of tensile strain. Taking into account the effects of stress on both the surface potential and the valence band, the relative variation of conductivity depends on both the thickness and the resistivity. Through this modulation, the effect of giant piezoresistance has been shown in p-type nanolayers. The results are in satisfying agreement with experimental data available for nanowires.

In conclusion, it is shown that the full-band Monte Carlo approach of semiclassical simulation semiconductor devices allows us to include all the complexity of the silicon band structures, especially in the presence of strain, and all non stationary transport phenomena which occur in modern nanodevices.

6. References

Aubry-Fortuna, V., Bournel, A.; Dollfus, P. & Galdin-Retailleau, S. (2006). Ultra-short n-MOSFETs with strained Si: device performance and the effect of ballistic transport using Monte Carlo simulation, *Semicond. Sci. Technol.*, Vol. 21, pp. 422-428.

Bir, G.L. & Pikus, G.E. (1974). *Symmetry and Strain-induced Effects in Semiconductors*, Wiley, New York.

Bufler, F.M.; Gautschi, R. & Erlebach, A. (2008). Monte Carlo stress engineering of scaled (110) and (100) bulk pMOSFETs. *IEEE Elect. Dev. Lett.*, Vol. 29, pp. 369-371.

Cardona M. & Pollak F.H. (1966). Energy-band structure of germanium and silicon : the *k.p* method. *Phys. Rev.*, Vol. 142, pp. 530-543.

Garnett, E.C. ; Tseng, Y.-C. ; Khanal, D.R. ; Wu, J. ; Bokor, J. & Yang, P. (2009). Dopant profiling and surface analysis of silicon nanowires using capacitance--voltage measurement. *Nature Nanotech.*, Vol. 4, pp. 311-314.

Ghetti, A.; Carnevale, G. & Rideau, D. (2007). Coupled Mechanical and 3-D Monte Carlo Simulation of Silicon Nanowire MOSFETs. *IEEE Trans. on Nanotech.*, Vol. 6, pp. 659-666.

He, R. & Yang, P. (2006). Giant piezoresistance effect in silicon nanowires. *Nature nanotech.*, Vol. 1, pp. 42-46.

Huet, K; Feraille, M; Rideau, D; Delaware, R.; Aubry-Fortuna, V.; Kasbari, M.; Blayac, S.; Rivero, C.; Bournel, A.; Tavernier, C.; Dollfus, P. & Jaouen, H. (2008a). Experimental and theoretical analysis of transport in uniaxially strained pMOSFETs. *Proceedings of the ESSDERC'2008*, pp. 234-237, Edimburg (United Kingdom), 15-19 september.

Huet, K. (2008). Modeling of carrier transport in sub-65nm CMOS transistors under mechanical stress (text in French), PhD Thesis, Université Paris-Sud, September 29.

Huet, K. ; Chassat, C. ; Nguyen D.-P. ; Galdin-Retailleau, S. ; Bournel, A. & Dollfus, P. (2008b). Full Band Monte Carlo study of ballistic effects in nanometer-scales strained P channel Double Gate MOSFETs. *Physica Status Solidi (c)*, Vol. 5, pp. 43-46.

ITRS (2008). http://www.itrs.net/Links/2008ITRS/Home2008.htm

Jungemann, C. ; Keith, S. ; Bartels, M. & Meinerzhagen, B. (1999). Efficient Full-Band Monte Carlo simulation of silicon devices. *IEICE Trans. Electron.*, Vol. E82-c, p. 870-879.

Laux, S.E. & Fischetti, M.V. (1991). Numerical aspect and implementation of the DAMOCLES Monte Carlo devices. Simulation program, In : *Monte Carlo device simulation: Full Band and Beyond*, K. Hess, pp. 1- 26, Kluwer, Dordrecht.

Leu, P.W. ; Shan, B. & Cho, K. (2006). Surface chemical control of the electronic structure of silicon nanowires: density functional calculations. *Phys. Rev. B*, Vol. 73, pp. 195320-195325.

Leu, P.W ; Svizhenko, A. & Cho, K. (2008). Ab initio calculations of the mechanical and electronic properties of strained Si nanowires. *Phys. Rev. B*, Vol. 77, pp. 235305-235319.

Luttinger, J.M. & Kohn, W. (1955). Motion of electrons and holes in perturbed periodic fields. *Phys. Rev.*, Vol. 97, pp. 869-883.

Ottaviani, G.; Reggiani, L.; Canali, C.; Nava, F. & Alberigi-Quaranta, A. (1975), *Phys. Rev. B*, Vol. 12, pp. 3318-3329.

Pham, A.T.; Jungemann, C.; Meinerzhagen, B. (2008). Deterministic multisubband device simulations for strained double gate PMOSFETs including magnetotransport. *Proceedings of the IEDM Technical Digest*, pp. 895-898, San Francisco (USA), 15-17 december.

Richard, S.; Aniel, F. & and Fishman, G. (2004). Energy-band structure of Ge, Si and GaAs. *Phys. Rev. B*, Vol. 70, p. 235204-235206.

Rideau, D.; Feraille, M.; Ciampolini, L.; Minondo, M.; Tavernier, C.; Jaouen, H. & Ghetti A. (2006). Strained Si, Ge and $Si_{1-x}Ge_x$ alloys modeled with a first-principles-optimized full-zone *k.p* method. *Phys. Rev. B,* Vol. 74, pp. 195208-195227.

Rim, K.; Chan, K.; Shi, L & al. (2003). Fabrication and mobility characteristics of ultra-thin strained Si directly on insulator (SSDOI) MOSFETs. *Proceedings of the IEDM Technical Digest*, pp. 311-314, Washington DC (USA), 8-10 december.

Rowe, A. C. H. (2008). Silicon nanowire feel the pinch. *Nature Nanotech.*, Vol. 3, pp. 311-312.

Saint Martin, J.; Bournel, A.; Dollfus, P. (2006). Comparison of multiple-gate MOSFET architectures using Monte Carlo simulation. *Solid-State Electr.,* Vol. 50, pp. 94-101.

Smith, C. S. (1954). Piezoresistance effect in germanium and silicon. *Phys. Rev.*, Vol. 94, pp 42-49.

Suthram, S; Ziegert, J.C.; Nishida, T. & Thomson, S.E (2007). Piezoresistance coefficients of (100) Silicon nMOSFETs measured at low ans high (≈ 1.5 GPa) channel stress. *IEEE Elect. Dev. Lett.,* Vol. 28, pp. 58-61.

Thompson, S.E.; Guangyu, S.; Youn Sung, C. & Nishida, T. (2006). Uniaxial-process-induced strained-Si: extending the CMOS roadmap. *IEEE Trans. Electron Dev,* Vol. 53, pp. 1010-1020.

Wang, E.X. ; Matagne, P. ; Shifren, L. ; Obradovic, B. ; Kotlyar, R. ; Cea, S. ; Stettler, M. & Giles, M.D. (2006). Physics of hole transport in strained Silicon MOSFET inversion layers. *IEEE Trans. on Electron Devices*, Vol. 53, pp. 1840-1851.

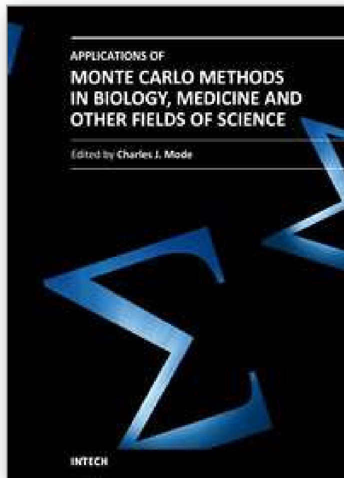

Applications of Monte Carlo Methods in Biology, Medicine and Other Fields of Science
Edited by Prof. Charles J. Mode

ISBN 978-953-307-427-6
Hard cover, 424 pages
Publisher InTech
Published online 28, February, 2011
Published in print edition February, 2011

This volume is an eclectic mix of applications of Monte Carlo methods in many fields of research should not be surprising, because of the ubiquitous use of these methods in many fields of human endeavor. In an attempt to focus attention on a manageable set of applications, the main thrust of this book is to emphasize applications of Monte Carlo simulation methods in biology and medicine.

How to reference
In order to correctly reference this scholarly work, feel free to copy and paste the following:

Valérie Aubry-Fortuna, Karim Huet, T.T. Trang Nghiêm, Arnaud Bournel, Jérôme Saint-Martin and Philippe Dollfus (2011). Strain Effects in p-type Devices using Full-Band Monte Carlo Simulations, Applications of Monte Carlo Methods in Biology, Medicine and Other Fields of Science, Prof. Charles J. Mode (Ed.), ISBN: 978-953-307-427-6, InTech, Available from: http://www.intechopen.com/books/applications-of-monte-carlo-methods-in-biology-medicine-and-other-fields-of-science/strain-effects-in-p-type-devices-using-full-band-monte-carlo-simulations

INTECH
open science | open minds

InTech Europe
University Campus STeP Ri
Slavka Krautzeka 83/A
51000 Rijeka, Croatia
Phone: +385 (51) 770 447
Fax: +385 (51) 686 166
www.intechopen.com

InTech China
Unit 405, Office Block, Hotel Equatorial Shanghai
No.65, Yan An Road (West), Shanghai, 200040, China
中国上海市延安西路65号上海国际贵都大饭店办公楼405单元
Phone: +86-21-62489820
Fax: +86-21-62489821

© 2011 The Author(s). Licensee IntechOpen. This chapter is distributed under the terms of the Creative Commons Attribution-NonCommercial-ShareAlike-3.0 License, which permits use, distribution and reproduction for non-commercial purposes, provided the original is properly cited and derivative works building on this content are distributed under the same license.
IntechOpen
IntechOpen